S1 ECHAMP Calibrations
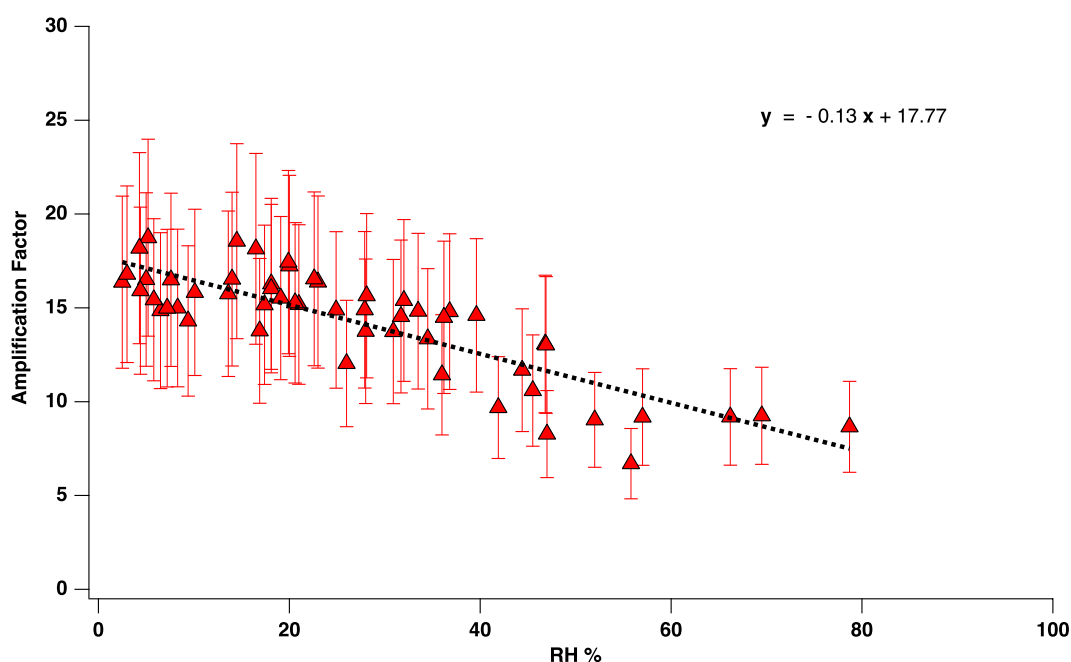
5   Figure S1 shows ECHAMP CH_3I calibration results. The amplification factor is equal to the amplified $[NO_2]$ signal divided by the calibrated XO_2 concentration. Ambient $[XO_2]$ was calculated by dividing the chemical amplification NO_2 signal by the RH-dependent amplification factor. The 2-sigma uncertainty of 34% was determined by combining in quadrature the error in calibration concentrations from the CH_3I method (a 20% uncertainty derived by Anderson et al. (2019)), the error in the calibration slope (Fig. S1) due to variability among individual calibration points (18%), and an additional uncertainty of 20% to reflect the

10   lack of information regarding HO_2 sampling losses (which ordinarily would be accounted for by H_2O photolysis calibrations).

Figure S1. ECHAMP calibration results for the FIREX 2018 campaign. Calibrations were conducted using the CH_3I based method. Indicated uncertainties are the ECHAMP measurement uncertainty of 27% (2 σ).

15

S2 Supplementary Measurements

       Photometric O_3 monitors can suffer from interferences from VOCs and PM that absorb or scatter 254 nm UV radiation (Huntzicker and Johnson, 1979). Recent measurements in concentrated BB plumes ($[CO] > 1$ ppmv) have shown that this interference can be large for certain types of photometric O_3 measurements (Long et al., 2021). The potential for our O_3

20   measurements, collected using a 2B-Tech Model 205 UV absorption monitor, to be impacted is low given that we sampled dilute BB plumes in this study (enhancements of PM < 30 μg m^{-3} and $[CO] < 0.1$ ppmv). Furthermore, a comparison of the 2B O_3 measurements to separate Ox measurements made by our novel ECHAMP XO_2 sensor demonstrate that interferences are negligible. ECHAMP measures Ox by mixing ambient O_3 with excess NO to form NO_2 which is later quantified by CAPS NO_2

instruments. The CAPS Ox results are based on the absorption of light at 450 nm and are expected to have minimal interferences as few compounds absorb in this region (Kebabian et al., 2008). We show a time series of 2B-Tech O_3 and ECHAMP Ox measurements in Fig. S2. The Ox measurements only include up to 2 ppbv NO_2, and a separate Ox time series derived from adding the 2B-Tech O_3 with TILDAS NO_2 data is shown for a more direct comparison to the ECHAMP CAPS Ox data. The 17 August period includes nearly 15 hours of background air and a nearly 3-hour smoke influenced period that started at 15:27 MDT and included enhancements of ~100 ppbv CO and ~20 µg m^{-3} organic PM. The 2B O_3 data during both the background and smoke periods, as well as for the entire campaign, agree with the CAPS Ox acquired from ECHAMP.
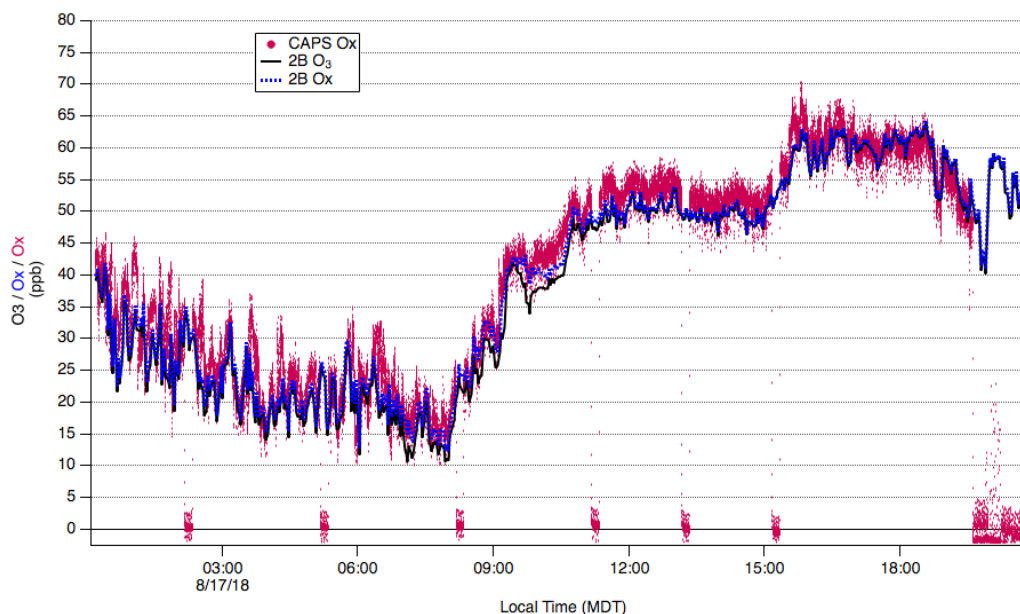
Figure S3 shows meteorological data.

Figure S2. Time series of 2B-Tech O_3, 2B-Tech derived Ox, and CAPS Ox data acquired from ECHAMP XO_2 sensor.
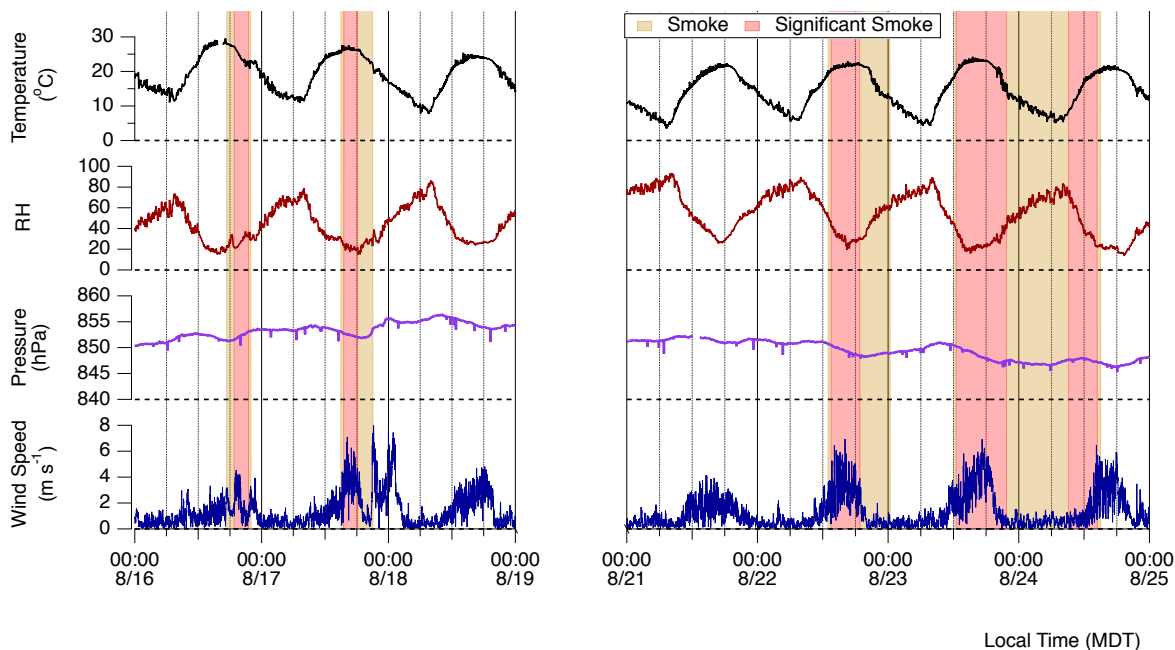

Figure S3. Meteorological data for the FIREX 2018 campaign. Periods of smoke are shaded as per Fig. 2 of the main text.

2

S3 HYSPLIT Back trajectories

NOAA Air Resources Laboratory HYbrid Single Particle Lagrangian Integrated Trajectory (HYSPLIT) (Stein et al., 2015) were used to speculate BB smoke sources for smoke influenced periods. Normal backward trajectories from the McCall, Idaho site coordinates of 44.8717º N and 116.1154º W were acquired using archived GDAS (1 degree, global, 2006 present) meteorology. Model vertical velocity was selected for the vertical motion method. Trajectories were acquired for all days of the field deployment. Files were acquired starting at 0:00 MDT with 48-hr back trajectories generated starting at each hour of the day. Height was selected at 10 m above ground level to best simulate site air. The height input was varied with values of 50m, 100 m, and 500 m for all dates to test possible interferences due to the mountain geography. Varying height had little impact overall with minimal changes observed for heights input 100 m and lower.

S4 Wildfire Sources

Maps that included HYSPLIT back trajectories and active wildfire locations were used to infer BB smoke sources for smoke influenced periods in McCall, Idaho. Results for the 17 August smoke event are presented in Fig. 1 of the main text and are discussed in depth there. Here, we share results for BB influenced periods of 16 August, 22 August, 23 August, 24 August.

The 16 August smoke event began at 18:48 MDT (with [HCN] > 1.0 ppb) and persisted until 21:55 MDT. This BB-influenced period coincides with the 18:00 MDT, 20:00 MDT, and 22:00 MDT back trajectories in Fig. S4. These trajectories are all similar and near a few active fires, while the earlier trajectories mostly avoid the active wildfires. Three wildfires are indicated in Fig. S4 - the Rattlesnake Creek Fire, the Mesa Fire, and the same unspecified wildfire suggested as responsible for the 17 August smoke event. This unspecified active wildfire is in closest proximity (within 5 km) for the trajectories of interest at 4-10 hrs backwards in time and is therefore the most likely source for BB smoke influence. However, the Rattlesnake Creek Fire may have also contributed as this fire was located farther downwind but within 20 km of trajectories. The Mesa Fire is the least likely source of BB smoke influence because it is farther than 20 km away of the trajectories of interest. The Mesa Fire is within close proximity of the 16:00 MDT trajectory only, prior to the BB smoke influenced period.
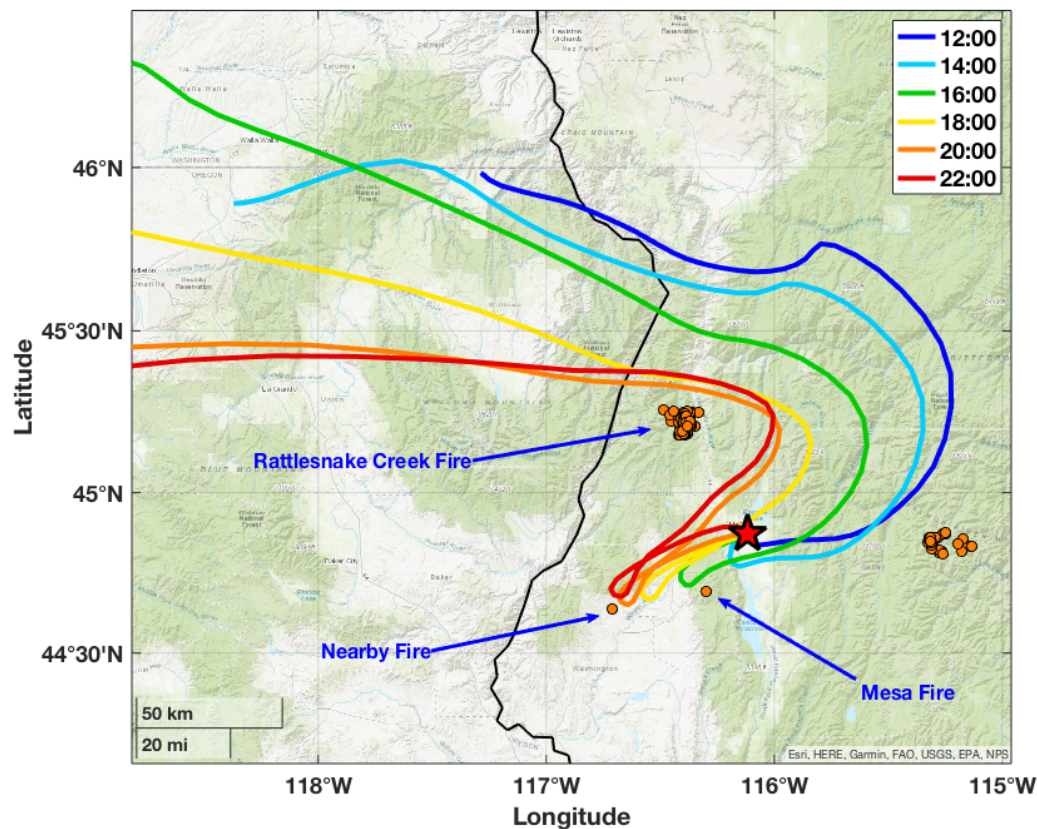
60

Figure S4. Bihourly HYPSLIT 48-hr back trajectories arriving at the McCall site (indicated by the red star) for the smoke influenced day of 16 August. Active wildfires of 15 August and 16 August are indicated by orange markers. Fire locations were retrieved using the NOAA Hazard Mapping System (HMS) (NOAA, 2021).

65   The trajectories for 22 August show site air being ultimately sourced from the northeast, though much of the transit time is spent directly east of the McCall site (Fig. S5). The Hazard Mapping System (HMS) wildfire data indicates wildfires mostly absent in this region for the 21-22 August date range. A few wildfires located directly east of McCall, Idaho were consistently observed during the field deployment (all wildfire HMS data is shown in Fig. 1 of main text). These fires, while undetected here, were detected both before and after this date range and include the Rabbit Foot Fire indicated in Fig. 1 of the main text as well as

70   two similarly sized fires located midway between the Rabbit Foot Fire and McCall, Idaho. These unspecified wildfires, even though they are undetected here, are a likely source as trajectories travel directly over the areas detected on other dates. The trajectories range 12-18 hours from these unspecified wildfires, though older smoke from a farther away source could have been sampled.
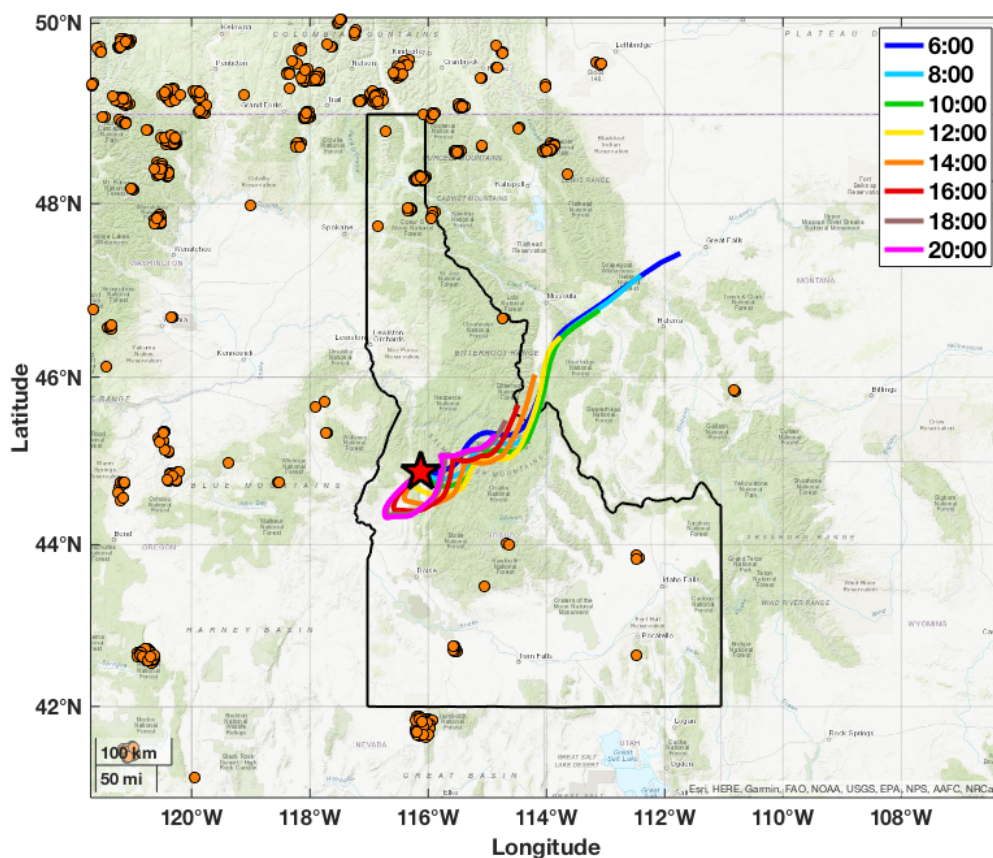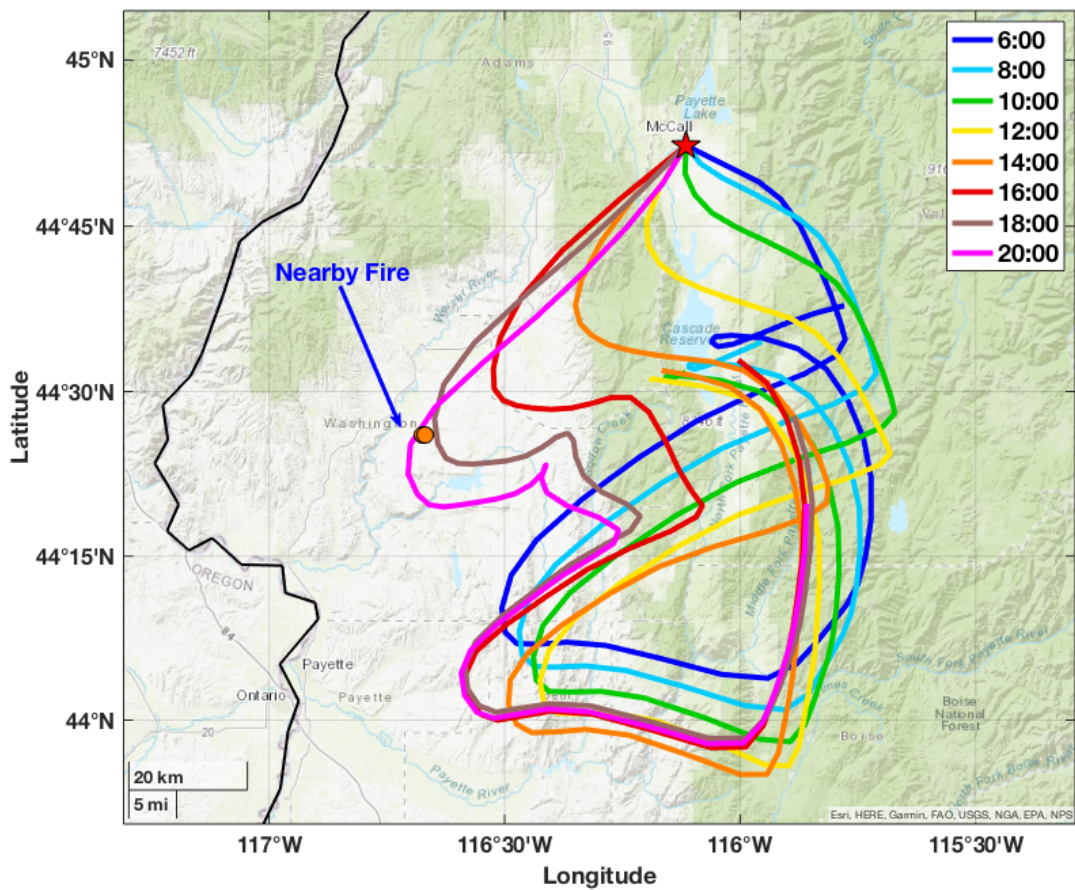
Figure S5. Same as Fig. S4 but for 22 August. Active wildfires (orange markers), which were acquired using HMS (NOAA, 2021), are shown for 21 August and 22 August.

Results for 23 August are shown in Fig. S6. Trajectories before 12:00 MDT show air was transported from the southeast, while trajectories starting at 12:00 MDTshow that air was transported from the southwest. This change in trajectories coincides with the BB influenced period beginning in the at 12:26 MDT and persisting through the end of the night (distinct BB smoke conditions with [HCN] > 1.0 ppb ended at 17:07 MDT but smoke tracers remained somewhat elevated after). One nearby fire was detected but is only in close proximity (within 5 km) to trajectories after the distinct BB influenced period. Conditions remained somewhat smoky after the distinct smoke period ended at 17:07 MDT, which this unspecified nearby fire likely contributed, with smoke tracers remaining elevated, but [HCN] falling just below 1.0 ppb. The Mesa Fire, however undetected here, may have contributed as many trajectories travel over or near the Mesa Fire areas detected on other days. As we are uncertain regarding the source of the sampled smoke, we suggest a moderate age of 12-18 hrs, though the plume impacting the site could be fresher with ages near 6 hrs.

Figure S6. Same as Fig. S4 but for 23 August. Active wildfires (orange markers), which were acquired using HMS (NOAA, 2021), are shown for 22 August and 23 August.

Figure S7 shows back trajectories for 24 August. Beginning with the 4:00 MDT trajectory, site air was sourced from Oregon. A cluster of fires likely responsible for the BB influenced period at 7:42 MDT is indicated in Fig. S7. The estimated transport time ranges 18-30 hours.
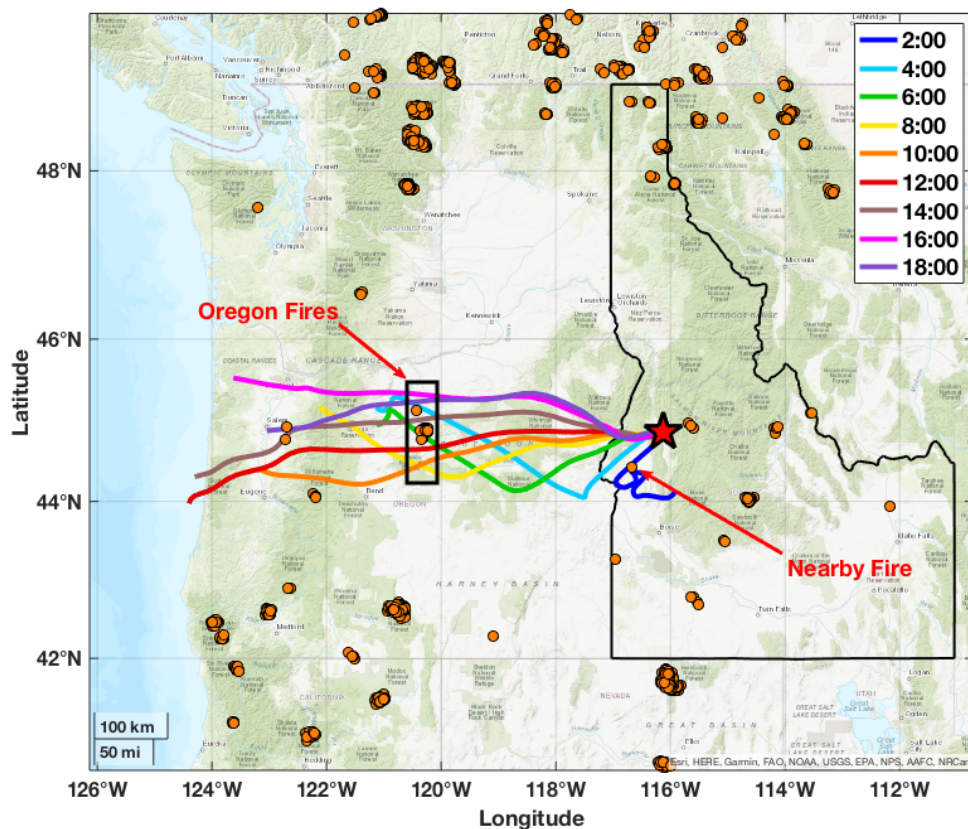
Figure S7. Same as Figures S4 but for 24 August. Active wildfires (orange markers), which were acquired using HMS (NOAA, 2021), are shown for 24 August and 25 August.

100

S5 Ozone Enhancement Ratios

Ozone enhancement ratios ($\Delta O_3/\Delta CO$) were determined using York bi-variate linear regressions. The $\Delta O_3/\Delta CO$ slopes for the 17 August and 24 August smoke events are shown in Fig. S8. The 16 August event is absent from Fig. S7 and was instead calculated by simple subtraction of a stable background period from a stable BB influenced period as recommended by Jaffe and

105   Wigder (2012). This avoided a temporary depletion in O_3 by ~20 ppbv during the BB influenced period.
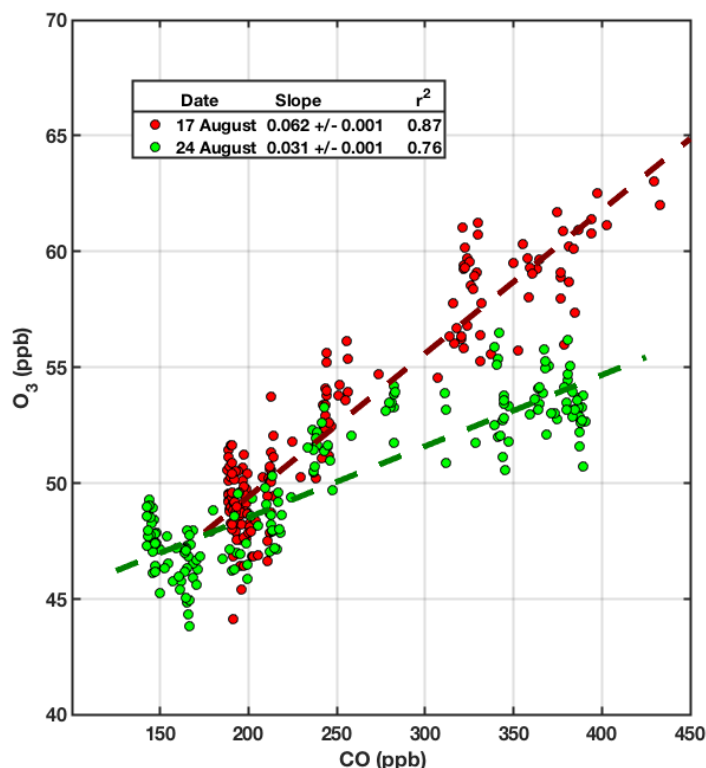
7

Figure S8. Comparisons of 2-minute O_3 and CO data that were used to derive biomass burning ozone enhancement ratios ($\Delta O_3/\Delta CO$) for the 17 and 24 August BB smoke events. Each set of data plotted was collected continuously and with the selected periods including 60 minutes of background air, a transition to or from BB smoke influence, and 60 minutes of significant BB smoke influence ([HCN]>1.0 ppb).

110

S6 Photolysis Frequencies

The National Center for Atmospheric Research (NCAR) Tropospheric Ultraviolet and Visible (TUV) model was used to acquire J_{NO2} and J_{O3} in 1-minute intervals. Notable TUV inputs included latitude and longitude of 44.9° and -116.1°, elevation of 1.53 km, the daily O_3 column value, surface albedo of 0.2, and single scattering albedo of aerosols of 0.99. Daily O_3 column values
115 were input as 295, 297, and 291 Dobson units for the 16 to 18 August period, respectively, and 316, 326, 306, and 315 for the 21 to 24 August period. These daily values were sourced using Ozone Monitoring Instrument (OMI) data.

The TUV photolysis outputs were then scaled using ARISense solar irradiance data in order to account for fluctuations due to clouds and BB smoke. TUV outputs were first synchronized in time to align with daily peak ARISense readings. We considered the ARISense solar cycle of 21 August as the standard profile as there were essentially no interferences. This standard
120 profile was scaled to match the peak values of each day and better align with overall ARISense observations. We then implemented any relative changes in solar irradiance measurements compared the standard profile into our TUV model J_{NO2} and J_{O3} outputs. ARISense data was not collected for most of 18 August so TUV outputs were not scaled.

S7 Model Description

The Framework for 0-D Atmospheric Modeling (F0AM) version 3.2 box model (Wolfe et al., 2016) was used to model
125 photochemistry and evaluate our peroxy radical measurements. In the main text, we briefly described the four chemical mechanisms that were employed. Three mechanisms (MCM-base, MCM-BBVOC, and MCM-BBVOC-het) involved using a

subset of the Master Chemical Mechanism (Jenkin et al., 2003;Saunders et al., 2003) version 3.3.1 (MCMv331) (Jenkin et al., 2015). The final mechanism was the base GEOS-Chem mechanism version 9-02 (Mao et al., 2013) with isoprene chemistry updates (Fisher et al., 2016;Marais et al., 2016;Travis et al., 2016;Kim et al., 2015). For all cases, the model was run using a model time-step of 2 minutes, with all observational constraints held constant throughout model steps. Concentrations of model intermediates were linked so that intermediates were initialized with concentrations predicted at the previous step.

Observational constraints included measured concentrations of water vapor, O_3, NO, NO_2, CO, CH_4, isoprene, monoterpenes, 2-methyl-3-buten-2-ol (MBO), methyl vinyl ketone (MVK), methacrolein (MACR), formaldehyde, acetaldehyde, ethane, ethyne, formic acid, acetic acid, acetone, MEK, benzene, toluene, C2 Benzenes, C3 Benzenes, and phenol, as well as temperature and pressure. As MVK and MACR are isomers, their Vocus measurement was split in a 0.34:0.66 ratio. This ratio was determined by box model acquired using the base MCM mechanism but with MVK and MACR constraints excluded. Total C2 and C3 benzene concentrations were assumed as mixtures of all isomers split into equal parts. For example, C2 benzene measurements were divided equally into MCM inputs of ethyl benzene, o-xylene, m-xylene, and p-xylene. For mechanisms that included manually written BB VOC chemistry (Coggon et al., 2019), additional observational constraints of furan, methyl furan, furfural, methyl furfural, guaiacol, and catechol were included. Since catechol and methyl furfural are isomers, the Vocus measurement of $C_6H_6O_2H^+$ was split into equal parts. For photolysis reactions, we constrained our derived values for J_{NO2} and J_{O3} (see Sect. 5). Other photolysis frequency values are then determined within F0AM based on these constraints. NO and NO_2 were constrained individually rather than fixing as total NOx. Fixing total NOx led to nearly identical daytime XO_2 predictions but with unrealistic nighttime XO_2 values. Unmeasured compounds were set to the default background concentration of 0 ppbv, and a first-order dilution was applied so that unmeasured compounds have a 24 hr lifetime.

Two instruments - Vocus and cTAG - measured many common species such as benzene, toluene, and isoprene. For these species, Vocus data were used as model inputs due to the faster Vocus time resolution and better overall data coverage for our periods of interest. While data coverage for other AML-based and site-based instruments was sufficient (data gaps < 60 minutes), there were two periods in which Vocus had extended gaps (> 6 hrs). Typical data gaps were shorter than 1 hour and filled via linear interpolation. However, these extended Vocus data gaps occurred on 17 August and 21 August and were filled with their corresponding cTAG measurements. Two compounds constrained in the model runs - 2-MBO and styrene - were unique to cTAG. However, cTAG data coverage had extended data gaps (e.g. missing a few entire days of interest). As 2-MBO and styrene correlated with isoprene and toluene, these cTAG compounds were assumed to maintain a constant ratio to their counterparts during periods of low cTAG data coverage.

The total $C_{10}H_{16}$ (monoterpenes) and C_5H_8 (mostly isoprene) concentrations measured by the Vocus PTR-MS were higher than those measured by the cTAG because the Vocus also measures isomers and artefacts of in-source fragmentation. Therefore, Vocus data was scaled to account for the fragmentation not observed by cTAG. Vocus isoprene was scaled by a factor of 0.66. Vocus total monoterpenes were scaled by a factor of 0.25 to match the trends observed for the sum of cTAG speciated monoterpenes. The F0AM monoterpene inputs for the chemical mechanisms used in this manuscript are partially speciated into α-pinene, β-pinene, and limonene. The total monoterpene signal was split into these categories based on the speciated cTAG observations. Along with α-pinene, β-pinene, and limonene, cTAG measured additional monoterpenes of 3-carene, β-phellandrene, and camphene. These additional monoterpenes were lumped into the F0AM relevant species based on their respective double bond positions, similar to the categorization suggested by Coggon et al. (2019). 3-carene was lumped with α-pinene, camphene was lumped with β-pinene, and β-phellandrene was lumped with limonene. The categories of α-pinene, β-pinene, and limonene maintained an average ratio of 0.49:0.42:0.09. As this ratio had little variation among all times with cTAG data, this ratio was applied to the Vocus total monoterpene measurement to include in F0AM model runs.

Heterogeneous uptake of HO_2 was included in the MCM-BBVOC-het mechanism by adding an additional HO_2 loss reaction that nets no product. The rate of this reaction was calculated with the following equation:

$$\frac{d[HO_2]}{dt} = -\frac{1}{4} \cdot \gamma \cdot c \cdot S \cdot [HO_2] \tag{1}$$

where γ represents the HO_2 uptake coefficient, c represents the mean molecular speed of HO_2, and S represents the aerosol surface area concentration (cm^2 m^{-3}). While c is derived from molecular weight and temperature, the parameters of γ and S are not as easily attainable. S was calculated from mass concentrations by multiplying by specific surface area (m^2 g^{-1}). We only considered organic aerosol mass concentrations for heterogeneous loss, which contributed the overwhelming majority of PM mass observations. The selected values of specific surface area and γ were held constant throughout model runs. The impact of γ and specific surface area on model predictions were tested with a separate GEOS-Chem mechanism that included this same heterogeneous HO_2 uptake chemistry. Figure S9 shows the impact of varying γ while specific area was held at our standard value of 2 m^2 g^{-1}. Figure S10 shows the impact of varying specific surface area while γ was held at our standard value of 0.2.

While observational constraints discussed within this section focus on MCM, GEOS-Chem constraints were comparatively limited. There were no observational constraints exclusive to GEOS-Chem. Rather GEOS-Chem lacked inputs for several species. This includes ethyne, all previously listed aromatic compounds, and BBVOCs.
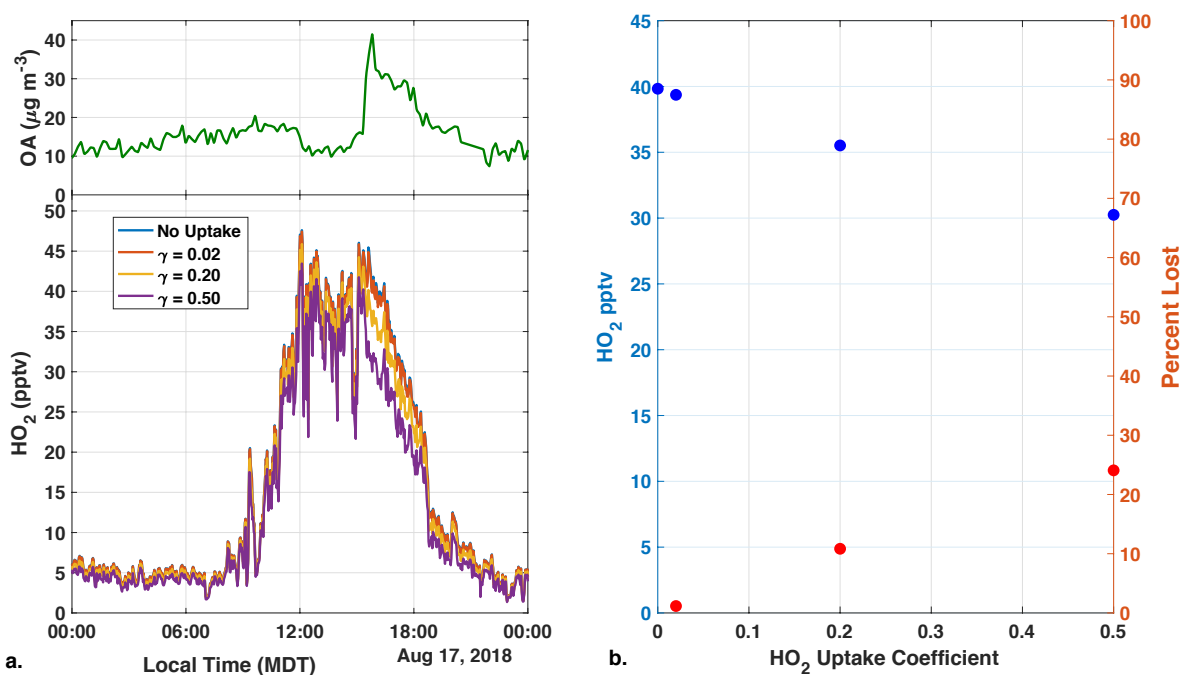

Figure S9. Impact of uptake coefficient on model predictions of HO_2. The heterogeneous uptake chemistry typically included in the MCM-BBVOC-het mechanism was included into the GEOS-Chem mechanism for this experiment. Panel A shows the time series of organic aerosol and model outputs of HO_2 with different uptake coefficients (γ). Panel B shows the impact of implementing heterogenous uptake on part of the 17 August BB influenced period of 15:40 MDT to 16:30 MDT. Blue markers represent predicted HO_2 concentration at each γ setting. The red markers are the percent loss in HO_2 relative to the base GEOS-Chem condition with no heterogeneous uptake.
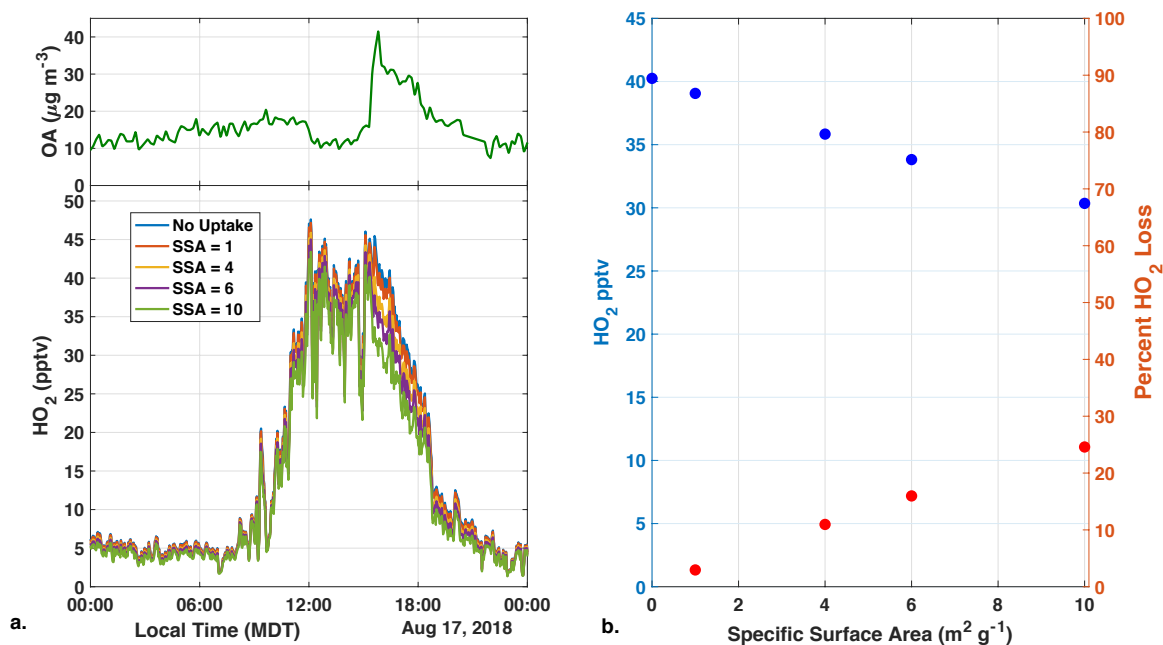
Figure S10. Impact of aerosol specific surface area on model predictions of HO_2. The heterogeneous uptake chemistry typically included in the MCM-BBVOC-het mechanism was included into the GEOS-Chem mechanism for this experiment. Panel A shows the time series of organic aerosol and model outputs of HO_2 with different aerosol specific surface areas (SSA) represented in the legend with units of $m^2 g^{-1}$. Panel B shows the impact of implementing heterogenous uptake on part of the 17 August BB influenced period of 15:40 MDT to 16:30 MDT. Blue markers represent predicted HO_2 concentration at each γ setting. The red markers are the percent loss in HO_2 relative to the base GEOS-Chem condition with no heterogeneous uptake.

S8 Supplemental Model Results

Supplemental model results, similar to MCM-BBVOC results shared in Fig. 6 of the main text, are shared in Figures S8-10. Each figure includes the model outputs of speciated peroxy radicals, [OH], and OH reactivity for unique mechanisms - MCM-base, MCM-BBVOC-het, and GEOS-Chem. While [OH] and OH reactivities remain similar across all MCM derived mechanisms, the GEOS-Chem results are most notably different. GEOS-Chem [OH] was on average ~75% greater than MCM-base predictions (note the extended [OH] y axis in Fig. S13. GEOS-Chem OH reactivity was limited due to the limited chemical species constrained. The most notable omission was BB VOCs, though other categories of MBO and aromatics are not represented as the measured species are not present in version of GEOS-Chem that was used.

To investigate the importance of HONO in the model results, we ran additional F0AM simulations using the GEOS-Chem mechanism with HONO concentrations constrained using a range of ΔHONO/ΔCO values and the measured CO mixing ratios. The raw enhancements in [HONO] for this event were 0.005 – 0.020 ppbv, 0.050 – 0.200 ppbv, and 0.150 – 0.600 ppbv when the ΔHONO/ΔCO value was set as 0.1 pptv ppbv^{-1}, 1.0 pptv ppbv^{-1}, 3.0 pptv ppbv^{-1}, respectively. XO_2 predictions for the 17 August BB event are shown in Fig. S14. In order for the model to produce the 15 pptv measured increase in [XO_2] we need to constrain HONO during BB influenced period using a rather large ΔHONO/ΔCO of 3.0 pptv ppbv^{-1} – much greater than the ΔHONO/ΔCO ratios observed for similarly aged plumes by Peng et al. (2020). While this value is likely unrealistic, larger ΔHONO/ΔCO have been reported by Peng et al. (2020) and can be implied up to 5.9 pptv ppbv^{-1}, though for considerably younger smoke plumes, using temperate forest emission factors (Akagi et al., 2011).

The sensitivity of model predicted XO_2 to the first-order dilution rate constant (k_{Dil}) was investigated using additional F0AM results acquired with the base GEOS-Chem mechanism (Fig. S15). Completely removing dilution allows for the further buildup of secondary species and higher predictions of [XO_2]. Increasing the rate constant from the standard 24-hr lifetime (k_{Dil} =

11

1/86400 s^{-1}) to a 6-hr lifetime (k_{Dil} = 4/86400 s^{-1}) leads to decreased XO$_2$ predictions that better align with the measured XO$_2$ values. The most important unmeasured radical precursors that are affected by this dilution setting are methyl glyoxal and glycolaldehyde. For results acquired using the MCM-BBVOC mechanism, the dilution setting is important for additional processes including limiting the buildup of photolabile carbonyls such as 4-oxo-2-pentenal (listed as C5DICARB within MCM).
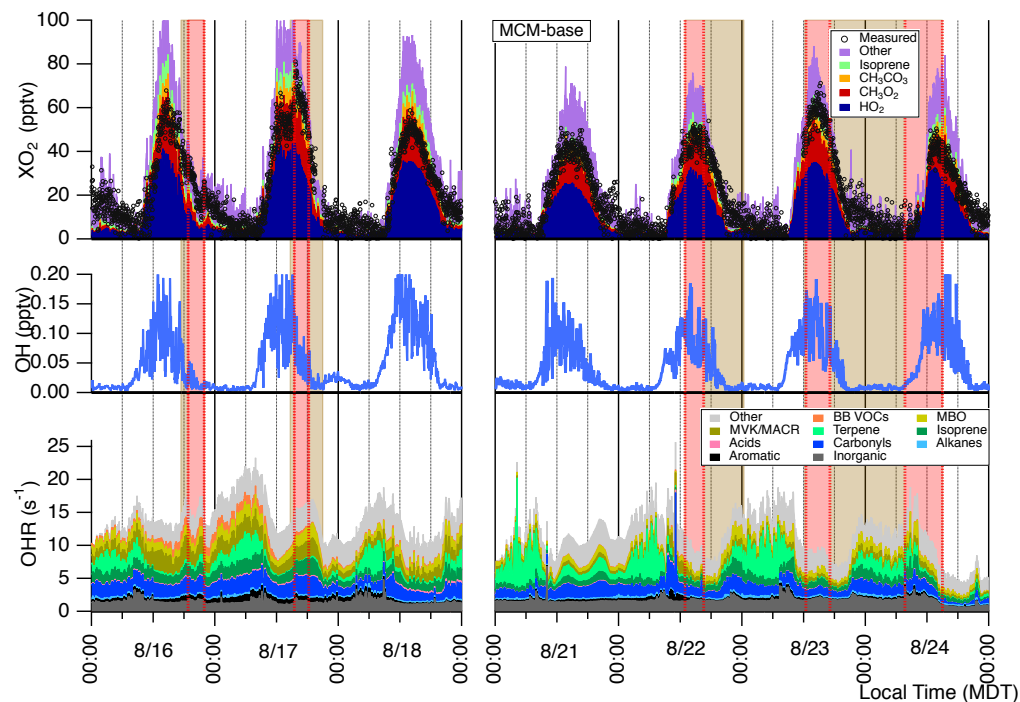
Figure S11. Time series of modeled OH, HO$_2$, speciated RO$_2$, and OH reactivity (OHR). These results were acquired using base MCM model. Periods of smoke are shaded as per Fig. 2 of the main text. Measured XO$_2$ is included as black markers for comparison.
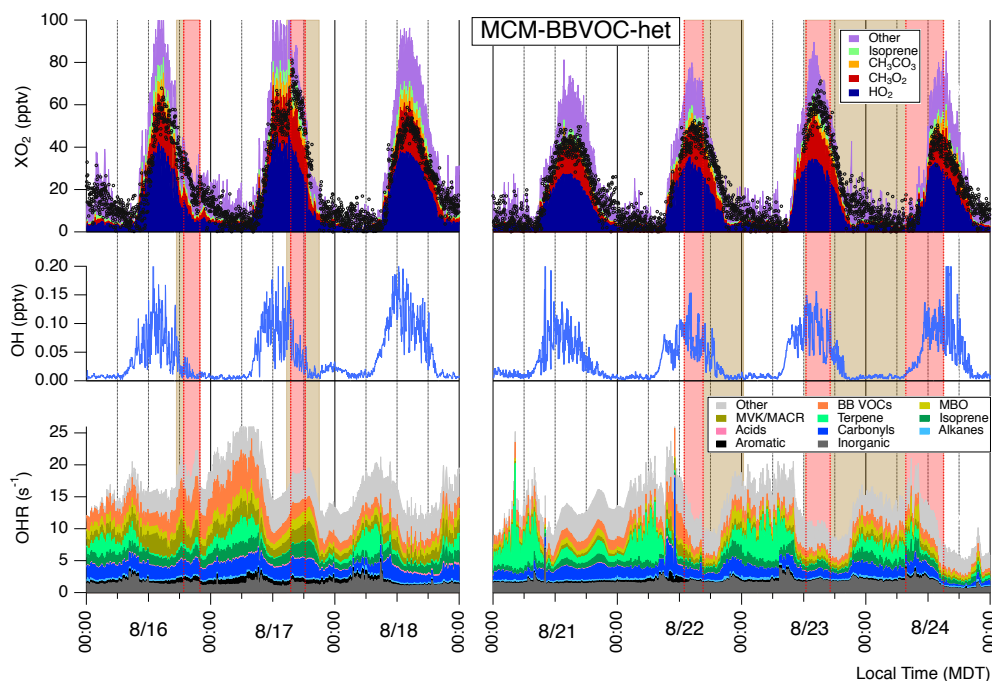

Figure S12. Same as Fig. S11 but model results were acquired with the MCM 3.3.1 mechanism including additional BB VOC chemistry and heterogeneous HO$_2$ uptake (MCM-BBVOC-het).
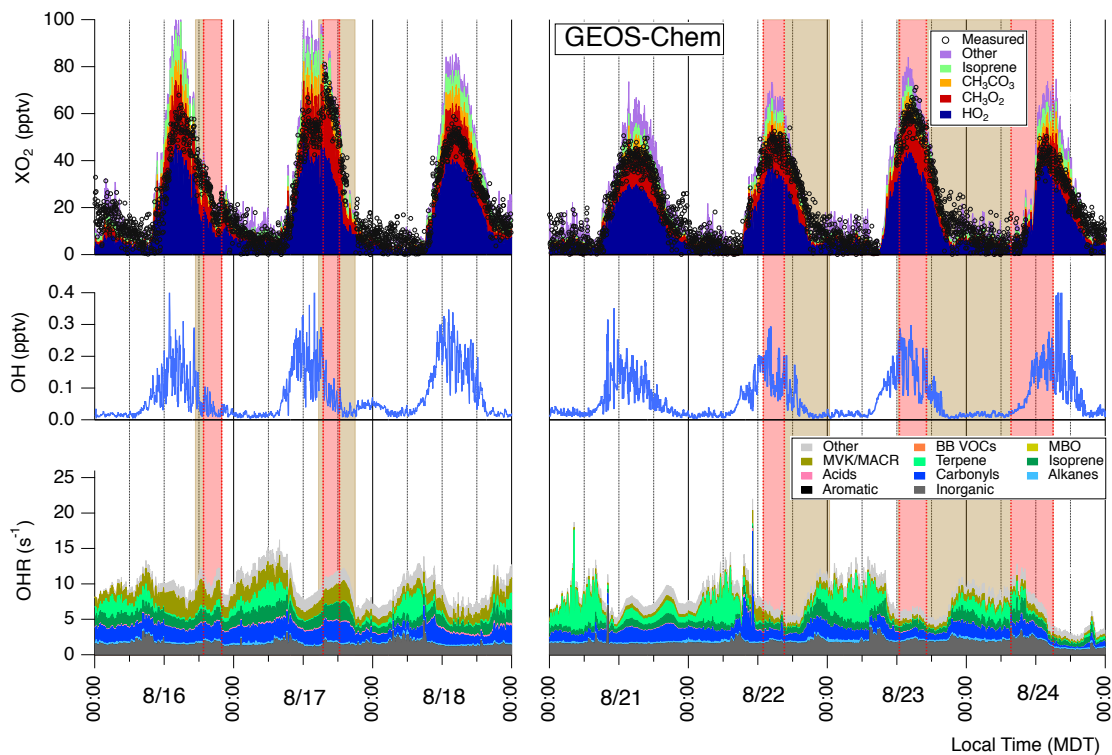
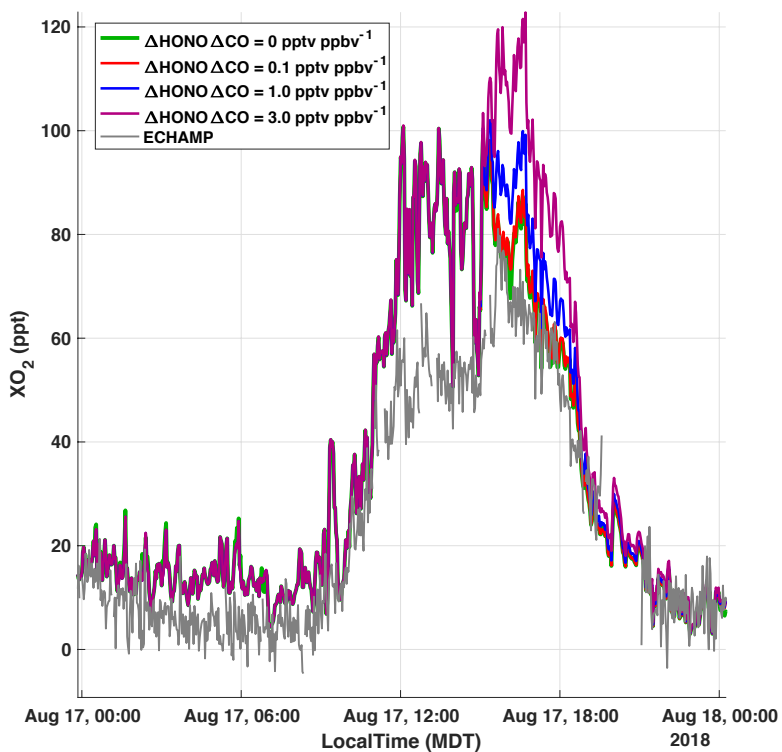**Figure S13.** Same as Fig. S11 but model results were acquired with the base version of GEOS-Chem.

Figure S14. F0AM XO_2 predictions with constrained HONO for 17 August period. Model results were obtained using the base version of GEOS-Chem. The initial HONO data constrained is based on the model outputs of HONO acquired using GEOS-Chem. Enhancements in HONO are then added for the 17 August BB event at 15:27 MDT using HONO enhancement ratios (ΔHONO/ΔCO).
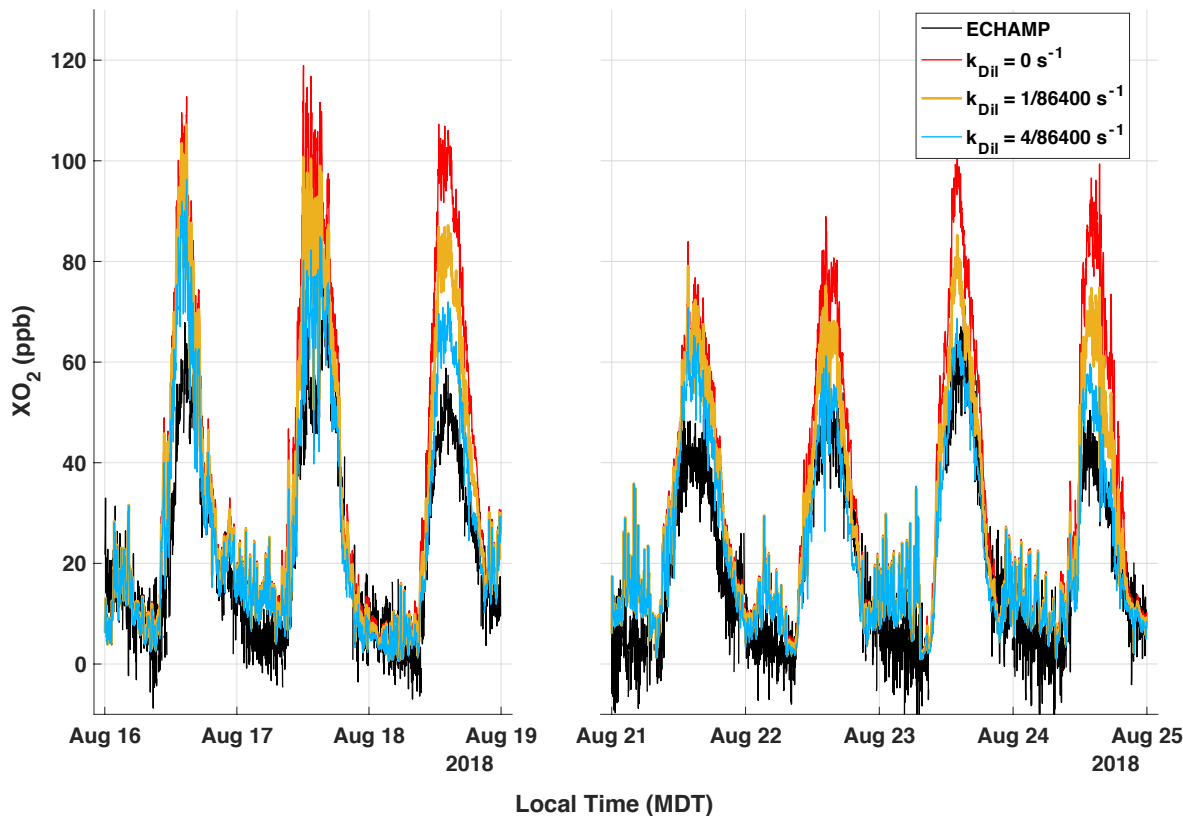
Figure S15. F0AM XO_2 predictions with varied first-order dilution rate constants (k_{Dil}) obtained using the GEOS-Chem mechanism. ECHAMP XO_2 measurements are included for comparison. Model predicted XO_2 results are shown for simulations that used the standard 24-hr dilution lifetime ($k_{Dil} = 1/86400$ s^{-1}), a 6-hr dilution lifetime ($k_{Dil} = 4/86400$ s^{-1}), and no dilution ($k_{Dil} = 0$ s^{-1}).

S9 Measured and Modeled HOx production

The 17 August period of BB influence had a distinct enhancement in [XO_2], though changes in P(HOx) appeared to be minimal. Figure S16 shows time series for HOx precursors of O_3 and HCHO along with J_{NO2} and water vapor during this event. A relative increase in [O_3] 27% (or 15 pptv) was counteracted by a similarly sized decline in water vapor. The result was a minimal impact on P(HOx).

Figure S17 shows the components of modeled HOx production, similar to Fig. 8 of the main text, for the date range of 21 through 24 August. The breakdown of HOx sources and sinks are generally consistent with that observed for 16 through 18 August. Appreciable heterogeneous losses are predicted midday on 23 and 24 August during BB influenced periods. On both of these days, heterogeneous losses approach termination rates equal to 10% of total HOx termination.
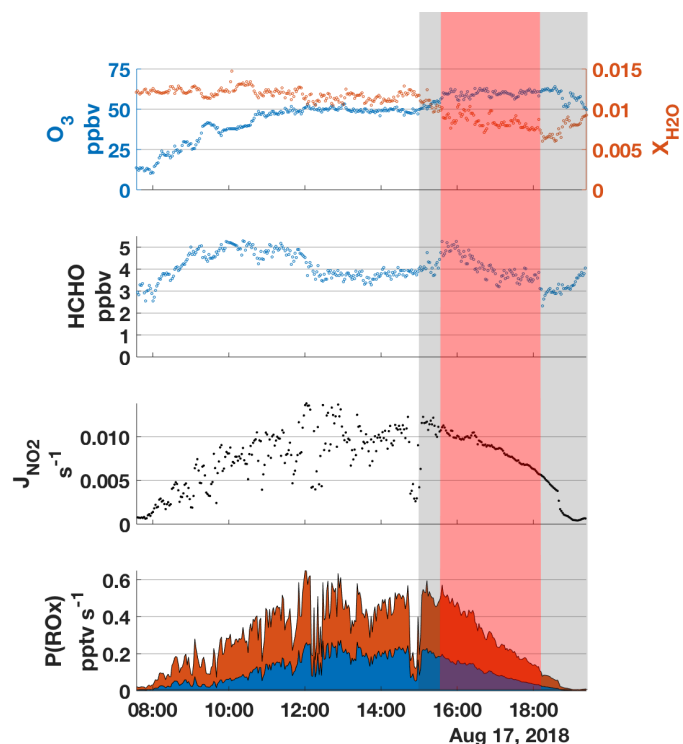
Figure S16. Investigation of P(ROx) on 17 August 2018. Time series of ROx precursors of O_3 and HCHO are included along with NO_2 photolysis and water mixing ration X_{H2O}. Periods of BB influence and significant BB influence ([HCN] >1.0 ppb) are shaded grey and red, respectively.
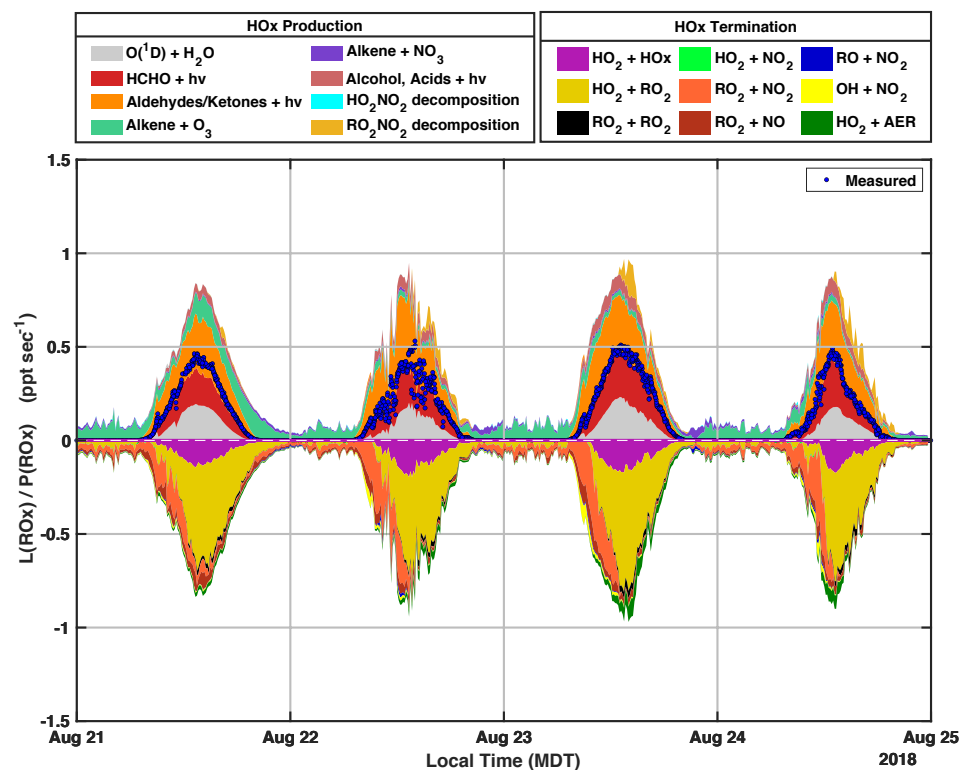
Figure S17. Modeled ROx production and termination for 21, 22, 23, and 24 August. The results provided were modeled with F0AM using the MCM-BBVOC-het mechanism. NROx termination L(ROx) and ROx production P(ROx) are separated into several straightforward categories as represented in their respective legends. For reversible processes, net rates are shown. Heterogenous HO_2 loss is represented by the HO_2 +

AER. P(ROx) derived from direct measurements, as presented in Fig. 3 of the main text, is shown in the main text and is represented by the blue markers. Modeled results were averaged from 2-minute intervals to 10-minute intervals, while the measured data is shown in 2-minute intervals.

References

Akagi, S., Yokelson, R. J., Wiedinmyer, C., Alvarado, M., Reid, J., Karl, T., Crounse, J., and Wennberg, P.: Emission factors for open and domestic biomass burning for use in atmospheric models, Atmospheric Chemistry and Physics, 11, 4039-4072, 2011.

Anderson, D. C., Pavelec, J., Daube, C., Herndon, S. C., Knighton, W. B., Lerner, B. M., Roscioli, J. R., Yacovitch, T. I., and Wood, E. C.: Characterization of ozone production in San Antonio, Texas, using measurements of total peroxy radicals, Atmospheric Chemistry and Physics, 19, 2845-2860, 2019.

Coggon, M. M., Lim, C. Y., Koss, A. R., Sekimoto, K., Yuan, B., Gilman, J. B., Hagan, D. H., Selimovic, V., Zarzana, K. J., and Brown, S. S.: OH chemistry of non-methane organic gases (NMOGs) emitted from laboratory and ambient biomass burning smoke: evaluating the influence of furans and oxygenated aromatics on ozone and secondary NMOG formation, Atmospheric Chemistry and Physics, 19, 14875-14899, 2019.

Fisher, J. A., Jacob, D. J., Travis, K. R., Kim, P. S., Marais, E. A., Miller, C. C., Yu, K., Zhu, L., Yantosca, R. M., and Sulprizio, M. P.: Organic nitrate chemistry and its implications for nitrogen budgets in an isoprene-and monoterpene-rich atmosphere: constraints from aircraft (SEAC4RS) and ground-based (SOAS) observations in the Southeast US, Atmospheric chemistry and physics, 16, 5969, 2016.

Huntzicker, J. J., and Johnson, R. L.: Investigation of an ambient interference in the measurement of ozone by ultraviolet absorption photometry, Environmental Science & Technology, 13, 1414-1416, 1979.

Jaffe, D. A., and Wigder, N. L.: Ozone production from wildfires: A critical review, Atmospheric Environment, 51, 1-10, 2012.

Jenkin, M., Saunders, S., Wagner, V., and Pilling, M.: Protocol for the development of the Master Chemical Mechanism, MCM v3 (Part B): tropospheric degradation of aromatic volatile organic compounds, Atmospheric Chemistry and Physics, 3, 181-193, 2003.

Jenkin, M., Young, J., and Rickard, A.: The MCM v3. 3.1 degradation scheme for isoprene, Atmospheric Chemistry and Physics, 15, 11433, 2015.

Kebabian, P. L., Wood, E. C., Herndon, S. C., and Freedman, A.: A practical alternative to chemiluminescence-based detection of nitrogen dioxide: Cavity attenuated phase shift spectroscopy, Environmental science & technology, 42, 6040-6045, 2008.

Kim, P. S., Jacob, D. J., Fisher, J. A., Travis, K., Yu, K., Zhu, L., Yantosca, R. M., Sulprizio, M., Jimenez, J. L., and Campuzano-Jost, P.: Sources, seasonality, and trends of southeast US aerosol: an integrated analysis of surface, aircraft, and satellite observations with the GEOS-Chem chemical transport model, 2015.

Long, R. W., Whitehill, A., Habel, A., Urbanski, S., Halliday, H., Colón, M., Kaushik, S., and Landis, M. S.: Comparison of ozone measurement methods in biomass burning smoke: an evaluation under field and laboratory conditions, Atmospheric Measurement Techniques, 14, 1783-1800, 2021.

Mao, J., Paulot, F., Jacob, D. J., Cohen, R. C., Crounse, J. D., Wennberg, P. O., Keller, C. A., Hudman, R. C., Barkley, M. P., and Horowitz, L. W.: Ozone and organic nitrates over the eastern United States: Sensitivity to isoprene chemistry, Journal of Geophysical Research: Atmospheres, 118, 11,256-211,268, 2013.

Marais, E. A., Jacob, D. J., Jimenez, J. L., Campuzano-Jost, P., Day, D. A., Hu, W., Krechmer, J., Zhu, L., Kim, P. S., and Miller, C. C.: Aqueous-phase mechanism for secondary organic aerosol formation from isoprene: application to the southeast United States and co-benefit of SO2 emission controls, 2016.

NOAA Hazard Mapping System Fire and Smoke Product: https://www.ospo.noaa.gov/Products/land/hms.html#data, access: 24 June 2021, 2021.

Peng, Q., Palm, B. B., Melander, K. E., Lee, B. H., Hall, S. R., Ullmann, K., Campos, T., Weinheimer, A., Apel, E., and Hornbrook, R. S.: HONO Emissions from Western US Wildfires Provide Dominant Radical Source in Fresh Wildfire Smoke, Environmental Science & Technology, 2020.

300 Saunders, S. M., Jenkin, M. E., Derwent, R., and Pilling, M.: Protocol for the development of the Master Chemical Mechanism, MCM v3 (Part A): tropospheric degradation of non-aromatic volatile organic compounds, 2003.

Stein, A., Draxler, R. R., Rolph, G. D., Stunder, B. J., Cohen, M., and Ngan, F.: NOAA's HYSPLIT atmospheric transport and dispersion modeling system, Bulletin of the American Meteorological Society, 96, 2059-2077, 2015.

305 Travis, K., Jacob, D., Fisher, J., Kim, P., Marais, E., Zhu, L., Miller, C., Wennberg, P., Crounse, J., and Hanisco, T.: NOx emissions, isoprene oxidation pathways, and implications for surface ozone in the Southeast United States, Atmos. Chem. Phys. Discuss., submitted, 2016.

Wolfe, G. M., Marvin, M. R., Roberts, S. J., Travis, K. R., and Liao, J.: The framework for 0-D atmospheric modeling (F0AM) v3. 1, Geoscientific Model Development, 9, 3309, 2016.